

Versatile Phenol-Incorporated Nanoframes for In Situ Antibacterial Activity Based on Oxidative and Physical Damages

Pei Liu, Yuzheng Wu, Babak Mehrjou, Kaiwei Tang, Guomin Wang,* and Paul K. Chu*

Gold nanoparticles (GNPs) with oxidase and peroxidase properties are great candidates for antibiotic-mimicking materials due to reactive oxygen species (ROS) production. However, the bioenzymic properties are not long-lasting due to the short lifespan of ROS and have only been observed from GNPs with a size of less than 20 nm, thus making the synthesis laborious and inefficient. Herein, GNPs with controllable size and effective ROS utilization are synthesized by an environmentally green process using natural phenols extracted from plants as the reducing and capping reagent. Functional metallic ions are chelated by taking advantage of the coordinating properties of phenols to form the versatile nanoframe (pGNP-Fe) that can self-assemble onto bacteria due to the inherent attraction rendered by phenols, and the physical pressure causes bacterial membrane damage. During internalization in bacteria, the cascade process resulting from the enzyme-like properties generates cytotoxic reactive ROS via oxidization, and the Fenton reaction enhances the antibacterial efficiency. This dual physical/chemical antibacterial process obviates the need for external antibiotics and antibacterial agents, which may otherwise pose toxicity in vivo. The fabrication strategy and materials properties described here provide insights into the design of antibiotic-mimicking materials based on enzymatic and physical effects.

instance, gold nanoparticles (GNPs) with unique optical, electronic, and biological properties have oxidase and peroxidase properties and can catalyze the production of ROS to kill bacteria.^[8] However, the catalytic properties are usually only found from small GNPs with a size of a few nanometers and the complex synthetic process requires harsh conditions as well as organic reducing reagents which can produce long-term toxicity.^[9] Hence, more benign and environmentally friendly methods are required for biomedical and clinical applications.

Phenols extracted from plants are eco-friendly and versatile agents in the synthesis and modification of biomaterials.^[10] For example, polyphenol-conjugated Au@AgNPs have been demonstrated to heal wounds.^[11] GNPs possess intrinsic oxidase properties because hydroxide peroxide (H_2O_2) can be generated with the proper physiological components,^[12] but the peroxidase properties of GNPs synthesized with phenols (pGNPs) have not been


observed from particles with a large size (>20 nm) because of the limited active sites.^[13,14] Since ROS decomposed from H_2O_2 by peroxidase is more lethal to bacteria, it is desirable to produce peroxidase-like properties on pGNPs to promote antibacterial efficiency. It has been observed that the active catechol moiety in phenols provides binding sites for ions such as Fe and the Fenton reaction produces ROS in the presence of H_2O_2 .^[15] Based on the preliminary results, it is possible to endow GNPs with both oxidase- and peroxidase-like properties. Besides, hydrogen bonds and π - π stacking between phenols and lipid bilayers of the bacterial membrane can foster assembly of phenols and the intermolecular force can further shorten the distance between the pGNP and bacteria,^[10] so that effective bacteria-killing can be accomplished with a small dose. Moreover, the absorbed pGNPs are expected to stretch and squeeze the membrane to produce mechanical deformation of the bacteria.^[16] However, there have been few studies on the catalytic properties of GNPs modified with phenols and the antibacterial properties and pertinent mechanisms are not well understood.

In this work, GNPs are prepared by a green reaction (sample designated as pGNP-Fe). Phenols act as both the reducing and capping reagents to form the gold core and provide coordination

1. Introduction

Bacteria resistance is becoming a global threat to human beings^[1] due to the overuse of antibiotics.^[2,3] Since most antibiotics kill bacteria via oxidative damage of DNA, RNA, and lipids by intracellular reactive oxygen species (ROS), alternative antibiotic-mimicking processes that can produce ROS efficiently are highly desirable.^[4-7] Owing to the short lifespan of ROS, enzyme-mimicking materials that trigger the formation of intracellular ROS in situ by taking advantage of endogenous “inventory” in the bacteria have attracted much interest. For

P. Liu, Y. Wu, B. Mehrjou, K. Tang, G. Wang, P. K. Chu
Department of Physics
Department of Materials Science and Engineering
and Department of Biomedical Engineering
City University of Hong Kong
Tat Chee Avenue, Kowloon, Hong Kong 999077, China
E-mail: guomiwang2-c@my.cityu.edu.hk; paul.chu@cityu.edu.hk

 The ORCID identification number(s) for the author(s) of this article can be found under <https://doi.org/10.1002/adfm.202110635>.

DOI: 10.1002/adfm.202110635

sites. The pGNP-Fe accumulates around the bacteria and the attached pGNP-Fe stretches the membrane to produce physical stress to the bacteria. At the same time, the enzyme-mimetic properties also trigger in situ generation of intracellular ROS to produce chemical stress in the bacteria. The synergistic chemical/physical interactions give rise to antibiotic-mimicking antibacterial properties. By producing the multifunctional nanoframe with phenols extracted from plants, the environmentally green synthetic strategy and attractive enzyme-like properties provide insights into the design of high-performance non-antibiotic antibacterial materials.

2. Results and Discussion

2.1. Synthesis and Characterization

Harsh conditions like a high temperature, strong reductants, or toxic surfactants are frequently needed in the traditional synthesis of GNPs and further modification is usually needed to reduce the toxicity.^[17] Hence, a green and simple approach is demanded by various biomedical applications. Here, catechin, a phytochemical belonging to tea polyphenols, is employed as a green reducing agent to synthesize GNPs. Apart from the reducibility, the active sites of catechin facilitate chelation of metal ions such as Fe³⁺ and the assembly driven by intermolecular interactions improves the absorption of GNPs onto microorganisms.^[18] In this way, the pGNP-Fe composite is expected to adhere to bacteria to produce an antibacterial

outcome by capitalizing on both the physical and chemical interactions.

The synthesis parameters are optimized by changing the concentration of catechin (0.05–0.8 mM) in the reaction. With a fixed concentration of chloroauric acid, aggregation is more likely to take place in the reaction with a catechin concentration higher than 0.4 mM after storing for 24 h (Figure S1, Supporting Information). The results indicate that this synthetic protocol is feasible if the concentration of catechin is controlled within a reasonable range. Figure 1a shows that pGNP-Fe with a size of about 50 nm is formed and distributed uniformly. The pGNP-Fe is enlarged slightly when the amount of catechin increases due to the capping oligomer layer. The slightly increasing size from pGNP-Fe1 to pGNP-Fe3 is confirmed by dynamic light scattering (DLS) (Figure 1b). The larger hydrodynamic size represented by DLS compared to that by transmission electron microscopy (TEM) can be explained by hydrogen bonding in the former case. The larger size from pGNP-Fe1 to pGNP-Fe3 results in a red-shift in the extinction spectra giving rise to the color change (Figure 1c).^[19] Compared to GNPs prepared with catechin alone (pGNP), addition of Fe³⁺ gives rise to a blue-shift from pGNP to pGNP-Fe (Figure 1c). This change in the surface plasmon resonance also verifies the good coordination between Fe³⁺ and nanoparticles.^[20] Compared to pGNP, all the pGNP-Fe groups show higher zeta potentials after Fe³⁺ chelation but a negative charge is still maintained (Figure 1d) indicating good stability. The FTIR spectra in the range between 1000–3500 cm⁻¹ are obtained to verify the chemical structure. The peak at 3300, 1614, and 1066 cm⁻¹ are attributed to the O–H bond, C=C ring

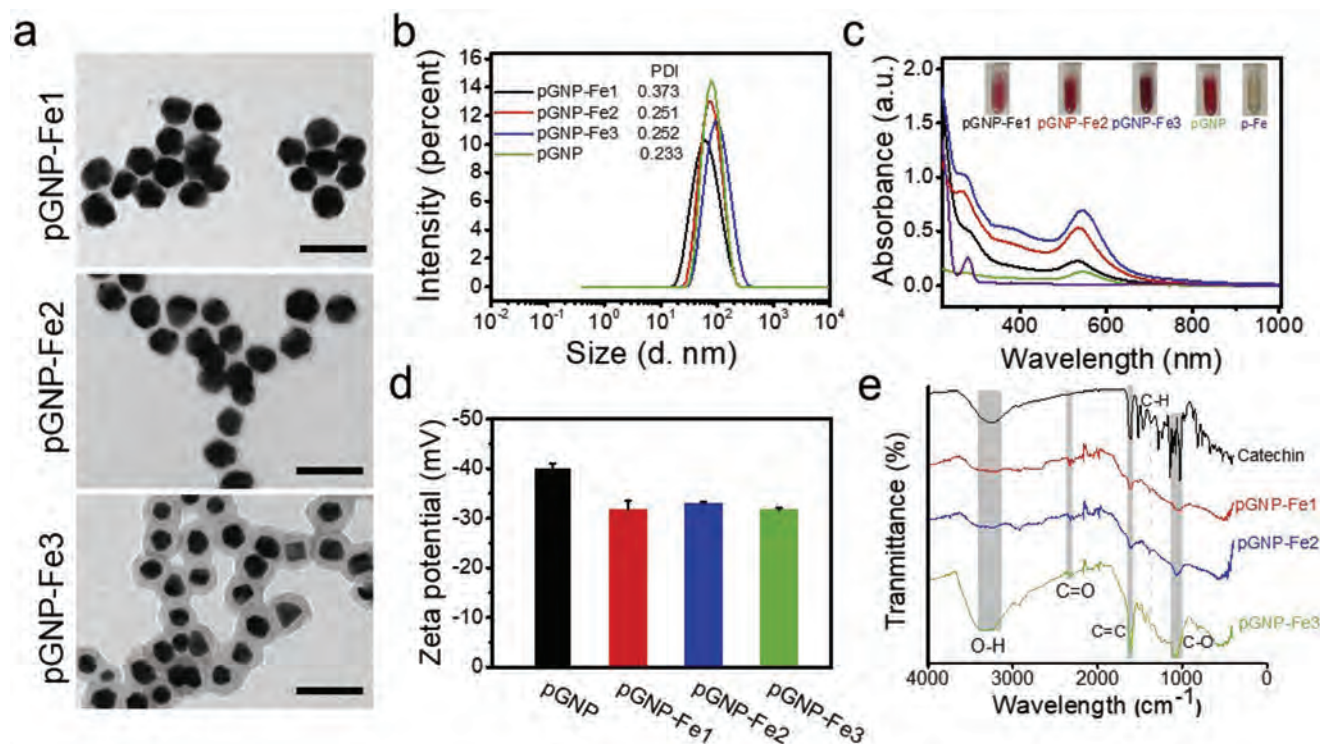


Figure 1. Characterization results: a) TEM images of the pGNP-Fe samples (scale bar = 200 nm); b) Hydrodynamic size of pGNP-Fe and pGNP shortly after synthesis; c) UV-vis spectra of pGNP, pGNP-Fe, and pFe with the optical images shown in the inset; d) Zeta potentials of pGNP and pGNP-Fe; e) The FTIR spectrum of catechin, pGNP-Fe1, pGNP-Fe2 and pGNP-Fe3.

stretching in polyphenols, and C–O in carboxylic acid, respectively. The absorption peak at 2323 cm^{-1} is associated with the stretching vibration of C=O, which indicates formation of the orthoquinone structure during oxidation of phenolic hydroxyls.

The stability of the colloid is evaluated by monitoring the hydrodynamic size and release of Fe^{3+} during storage overnight at room temperature. Both the hydrodynamic size and polydispersity index (PDI) of pGNP and pGNP-Fe change only slightly implying that the solutions are stable and the pGNP-Fe disperses well in the colloid (Figures S2a,b, Supporting Information). The concentration of released Fe^{3+} is below the detection limit of the technique further corroborating the structural stability (Figure S2c, Supporting Information). These results illustrate the successful synthesis of pGNP-Fe by this green and simple method involving phenols and Fe^{3+} .

2.2. Oxidase- and Peroxidase-like Properties

The oxidase-like and peroxidase-like properties are crucial to the antibacterial ability. Ascorbic acid (AA) with a characteristic absorption peak at 250 nm is chosen as the model to evaluate the oxidase-like ability and the oxidase ability is reflected by decreased absorption intensity arising from consumption of AA. The pGNP and pGNP-Fe samples show oxidase functions as revealed by the significantly reduced absorbance (Figure 2a and Figure S3, Supporting Information). A small change is detected from pFe suggesting the absence of oxidase func-

tions. The oxidase-like ability can thus be attributed to the GNPs which can take advantage of O_2 in the microenvironment to produce H_2O_2 oxidizing AA to decrease the absorbance.^[21] Hence, the oxidase-like ability is observed from pGNP and pGNP-Fe, but not pFe. Oxidation in pGNP-Fe is more rapid than that in pGNP as verified by the more rapid drop in the absorbance in the former case. Therefore, chelation of Fe^{3+} spurs production of H_2O_2 which is determined quantitatively as shown in Figure 2b. The concentration of H_2O_2 is $22\text{ }\mu\text{M}$ in pFe. It increases to $25\text{ }\mu\text{M}$ in pGNP and further increases to $27\text{ }\mu\text{M}$ for pGNP-Fe1 and pGNP-Fe2 consequently supporting our hypothesis. As a self-sufficient mini-factory, the microorganism itself is equipped with a set of outfits to produce essential items to keep homeostasis.^[22] Therefore, endogenous compounds can be oxidized efficiently upon contact with the synthesized pGNP-Fe and as a result, H_2O_2 is produced in situ and provides another source for the production of intracellular ROS.

H_2O_2 can be decomposed biologically into ROS by catalase and the rate-determining step involves O–O bond breaking.^[23] The peroxidase-like properties are evaluated according to the following two aspects. Firstly, the samples are used to catalyze the oxidation of TMB in the presence of H_2O_2 . Catalytic oxidation of TMB is reflected by the absorbance increase at 652 nm and compared semi-quantitatively (Figure 2c and Figure S4, Supporting Information). No obvious catalytic activity is detected from the pGNP group, while TMB is oxidized by H_2O_2 in less than 10 min due to catalysis of pFe.

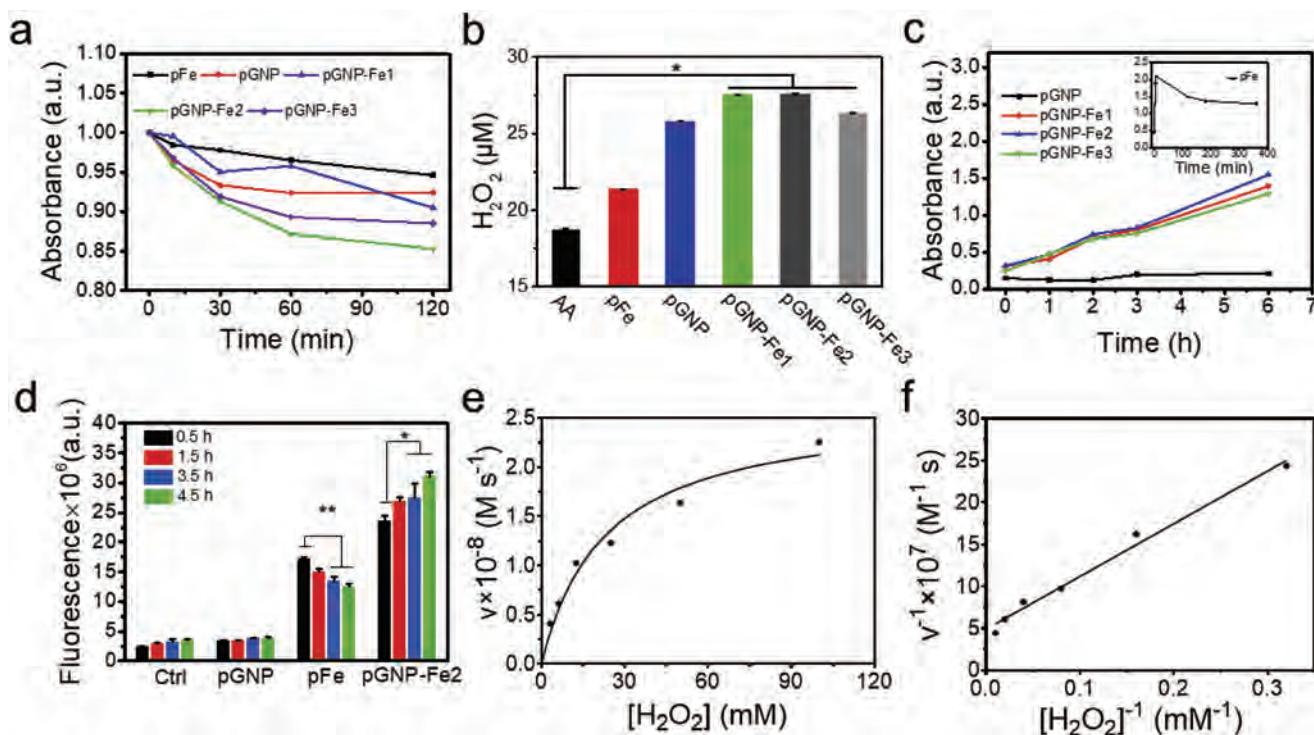


Figure 2. Oxidase- and peroxidase-like properties and enzyme kinetics investigation: a) Relative absorbance curves of AA interacting with the different samples for different durations; b) Concentrations of H_2O_2 under different conditions; c) UV-vis absorbance curves of TMB with H_2O_2 interacting with the different specimens for different durations; d) Fluorescence intensity of ROS under different conditions at different time points; e) Michaelis-Menten fitting and f) Lineweaver-Burk fitting for different H_2O_2 concentrations and 1 mM TMB (pH = 4.2) (* and ** denote $p < 0.05$ and $p < 0.01$, respectively).

Moreover, oxidation of the pGNP-Fe₂ group lasts for 6 h indicating a robust and long-lasting catalytic process. The absence of catalytic activity of pGNP is probably due to the large particle size of more than 20 nm, because strong catalase-like properties are usually detected from noble nanoparticles less than 10 nm in size.^[8] In contrast, the Fenton reaction takes place in the other two groups. Fast oxidation which lasts for less than 10 min and steady catalytic oxidation that lasts for more than 6 h are observed from pFe and pGNP-Fe, respectively. The enhanced long-term catalytic activity may contribute to the surface plasmon-enhanced Fenton reaction.^[24]

The catalytic ability is further verified by monitoring the production of ROS at different time points (Figure 2d). The generation of ROS is in line with catalytic oxidation. pGNP shows a negative ROS signal at the same level as the negative control group and obvious ROS signals are detected from pFe and pGNP-Fe₂. However, the ROS intensity of pFe declines quickly, whereas that of pGNP-Fe₂ is above 2E7 and continues to increase. This is consistent with catalytic oxidation shown in Figure 2c, demonstrating that chelation of Fe³⁺ with the capped phenols endow the GNPs with both oxidase- and peroxidase-like properties, thereby facilitating production of a large amount of ROS on the nanoparticles with a large size in addition to the continuous supply of H₂O₂ by the gold core. Compared to the harsher conditions such as a high temperature required for the formation of gold nanoparticles with a smaller size,^[17] our synthetic strategy is both environmentally friendly and energy-saving, while the enzyme-mimicking ability is well maintained.

The steady-state kinetics and nanoenzymatic properties of pGNP-Fe₂ are determined by the Beer-Lambert law^[25] and H₂O₂ is chosen to explore the catalytic kinetics. The change in the absorbance at 652 nm versus H₂O₂ concentration is monitored (Figure S5, Supporting Information) and the typical Michaelis-Menten fitted curve is obtained (Figure 2e). According to the fitted Lineweaver-Burk curve (Figure 2f), the Michaelis-Menten constant (K_m) and maximum velocity (V_{max}) are 23 mM and $2.61 \times 10^{-8} \text{ M s}^{-1}$, respectively (Table S1, Supporting Information). A comparison with Horseradish peroxidase (HRP) as the standard peroxidase and other Fe-based peroxidases such as Fe₃O₄ is made and pGNP-Fe₂ shows a K_m value that is 85% smaller than that of Fe₃O₄ MNPs, indicating that pGNP is a more favorable peroxidase with a higher affinity to H₂O₂.

2.3. Antibacterial Properties

Antibacterial efficiency: First of all, the general antibacterial properties are evaluated using common bacteria such as *E. coli* and *S. aureus*. Owing to the similar enzyme-like properties of the pGNP-Fe groups, pGNP-Fe₂ with the highest ROS generation is selected in our investigation. The antibacterial rate against *S. aureus* is slightly lower than that against *E. coli* after 24 h (Figure S6, Supporting Information) and therefore, *E. coli* is chosen to explore the antibacterial mechanism. In the 24 h period, pGNP-Fe₂ exhibits a 100% antibacterial rate and the other two groups also can kill 80% of the *E. coli* (Figure S7, Supporting Information). To further investigate the antibacterial behavior and mechanism, the bacteria after cultivation for 1 h and 3 h are examined in detail (Figures 3a,b). pGNP-Fe₂

fares best at both time points (68% after 1 h and 88% after 3 h), followed by pFe (33% after 1 h and 49% after 3 h) and pGNP (26% after 1 h and 43% after 3 h) (Figures 3a,b). The antibacterial rates increase significantly with time for pFe ($p = 0.008$) and pGNP-Fe₂ ($p = 0.03$), but no significant difference is found from pGNP ($p = 0.072$). This trend is consistent with the real-time antibacterial results by live/dead staining (Figure 3c).

Membrane change: The bacterial membrane integrity is evaluated to investigate the effects of different groups. The permeability of the outer *E. coli* membranes is evaluated by 8-Anilino-1-naphthalenesulfonic acid (ANS) and a higher fluorescence intensity indicates increased permeability. As shown in Figure 3d, the pGNP-Fe₂ group shows elevated permeability than both the pGNP and pFe groups. The larger permeability is expected to decrease the membrane potential, which is verified by the results in Figures 3e,f. The enhanced permeability is believed to foster the interaction between bacteria and samples which is evaluated by scanning emission microscopy (SEM). As shown in Figure 3g, the bacteria in the control group have the typical rod shape. The invagination of membranes is observed in the pFe group and attachment of pGNP onto bacterial membranes indicates physical pressure. The bacteria on pGNP-Fe₂ are surrounded by more nanoparticles than pGNP and show the most severe physical damage among the three groups. Although both the bacteria membrane and pGNP-Fe show negative potentials (Figure 1d), non-covalent interactions including hydrophobic interactions, hydrogen bonds and π - π stacking between the phenols and lipid bilayers of the bacteria contribute more than the electrostatic force to foster self-assembly of bacteria for pGNP-Fe.^[26,27] The membrane change is also confirmed by TEM. The bacterial membrane of pFe is deformed mildly but a large blank area is found from the pGNP-Fe₂ group reflecting serious damage to the bacterial membrane and outflow of internal substances (arrows in Figure 4a). Combined with the bacterial membrane assessment, it can be concluded that the membrane damages in the pGNP and pFe groups are caused primarily by physical pressure and chemically disruption by catechol, respectively.

Intracellular change: After confirming the influence on the membrane of bacteria, the intracellular components are investigated further. Obvious black bulk can be found from the pGNP-Fe₂ and pGNP groups and the elemental distributions are determined by EDS (Figure 4b). Compared to the control group, the amount of Au of the pGNP group increases by almost five times and both Fe and Au of the pGNP-Fe₂ group increase by almost six folds thereby furnishing direct evidence of internalization of pGNP and pGNP-Fe₂ in the bacteria. The oxidase and peroxidase functions of the internalized pGNP-Fe are expected to generate ROS in situ during interaction with bacteria. Overloaded oxidative stress induced by ROS is lethal to microorganisms and is the core mechanism in antibiotic- or non-antibacterial therapy.^[2] The intracellular ROS level is monitored qualitatively by fluorescent imaging and quantified. Green dots are barely found from pGNP and the amounts of bacteria with positive ROS signals increase in the order of pFe < pGNP-Fe₂ (Figure 4c). Quantitatively pGNP shows a similar ROS level as the negative control group, but positive ROS signals are detected from pFe and pGNP-Fe₂. Compared to the two latter groups, the intracellular ROS levels of pFe and

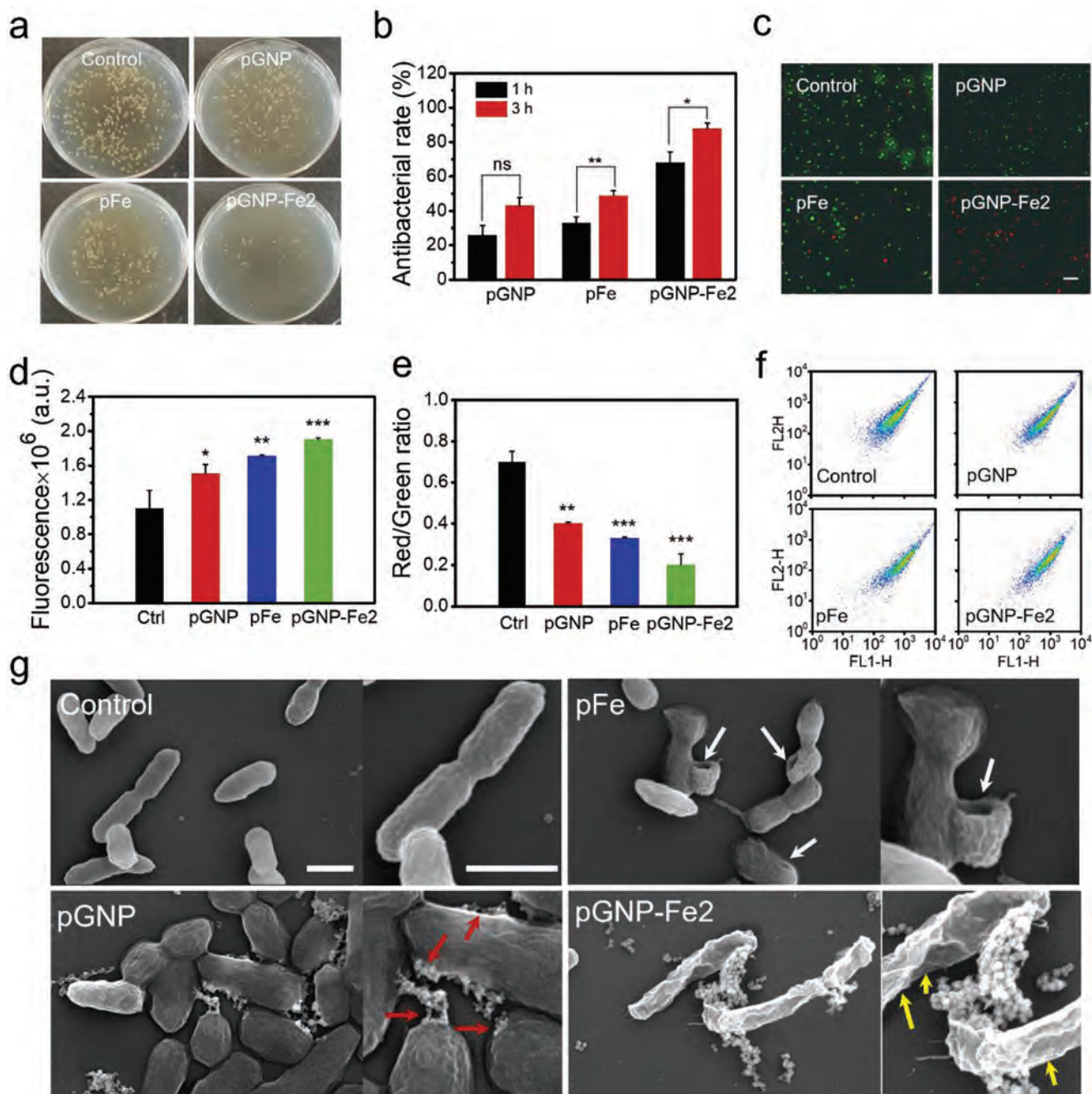


Figure 3. Antibacterial efficiency and interactions with bacterial membranes: a) Optical images of colony forming units (CFU) of *E. coli* after treatment for 3 h, $[Au] = 40 \text{ mg L}^{-1}$, $[Fe^{3+}] = 0.8 \text{ mg L}^{-1}$ for pFe; b) Calculated antibacterial rates after 1 h and 3 h; c) Live/dead fluorescence images (scale bar = 20 μm); d) Outer membrane permeability of *E. coli* for different treatments; e) Membrane potentials presented as red/green ratios and f) flow cytometry dots for the different treatments; g) SEM images of the bacteria on different samples (scale bar = 1 μm) (*, **, and *** denote $p < 0.05$, 0.01, and 0.001, respectively).

pGNP-Fe2 are similar in the beginning, except that the former declines quickly and the latter maintains a comparatively high level for 4 h (Figure 4d). The observation is consistent with the peroxidase-like properties described above (Figure 2d). It can be ascribed to the self-supply of H_2O_2 and the oxidase properties endow pGNP-Fe with the long-lasting catalytic activity. On the other hand, catalytic oxidation in pFe is restricted by the limited amount of H_2O_2 in the beginning.

3. Discussion

Most reported Fe-based nanoenzymes are synthesized with organic reagents which cost more and are less environmentally friendly.^[28,29] In this work, phenol as a multifunctional reagent is chosen for green synthesis of GNP, in which phenol acts as the reductant and chelating agent because it can also self-assemble on microorganisms and cells.^[18,30] To the best of

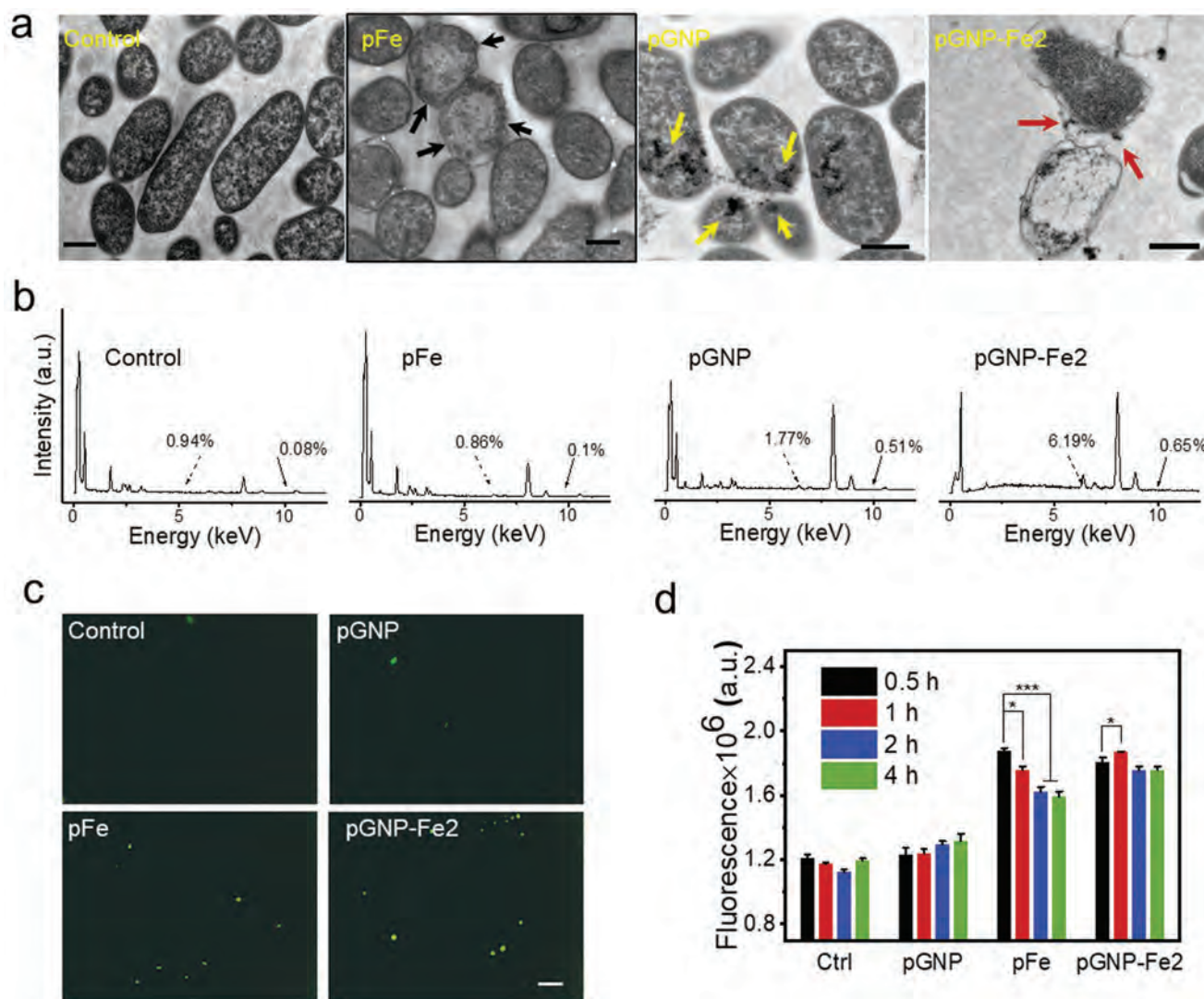


Figure 4. Intracellular change: a) TEM images of different groups (scale bar = 500 nm); b) EDS spectra of different groups with the dashed line indicating the weight % of iron and a solid line indicating the weight % of gold; c) ROS fluorescence images (scale bar = 20 μ m); d) Intracellular ROS levels of pGNP, pFe, and pGNP-Fe2 (* and *** denote $p < 0.05$ and $p < 0.001$, respectively).

our knowledge, chelation of Fe^{3+} with GNPs synthesized with phenols (pGNP) has not been reported before. The pGNPs possess intrinsic oxidase properties but little peroxidase properties because of the limited active sites arising from large size.^[12–14] Here, we make use of the active sites on phenol to coordinate Fe^{3+} to pGNP and both oxidase-like and peroxidase-like properties are achieved with pGNP-Fe with a large size, which is desirable for bacteria-killing applications. On the other hand, the short lifespan of ROS usually hinders the process, but pGNP-Fe2 possessing peroxidase-like properties revealed by our experiments generates ROS continuously. This phenomenon is different from that observed from other iron-based nanoenzymes^[31,32] and serves to enhance the utilization of the nano-frame. Furthermore, the Fenton reaction complements and is quite critical to the green synthesis strategy.

Our results provide clues concerning the different antibacterial mechanisms of the three different groups of samples. pGNP possessing oxidase-like properties only produces

a limited amount of H_2O_2 , which can hardly produce enough intracellular ROS without the contribution of oxidative stress. In comparison, the nanoparticles adhered to the bacterial membrane produce physical stretching and weak antibacterial effects.^[33] pFe can penetrate the bacteria membrane to trigger the Fenton reaction by utilizing the small amount of intracellular H_2O_2 .^[34] However, the limited amount of intracellular H_2O_2 runs out soon and consequently, the transient oxidative stress can only kill a small number of bacteria. On the other hand, the excellent antibacterial ability of pGNP-Fe2 can be explained by the synergistic effects rendered by the physical and chemical interactions as demonstrated unequivocally by our data. First of all, effective adsorption of nanoparticles on the bacteria increases the stretching stress leading to severe physical damage of the membrane. Second, accumulation of pGNP-Fe2 in the intracellular part enhances the oxidase capacity of the gold nanoparticles and peroxidase functions via the Fenton reaction. The catalytic properties are also chemically

demonstrated by studying and comparing the enzymatic kinetics. A sufficient amount of H_2O_2 is produced steadily to catalytically produce ROS in situ by the Fenton reaction, consequently producing stable and long-lasting oxidative stress to kill more bacteria. This fundamental study of the catalytic and antibacterial behavior enriches our understanding of the antibacterial mechanism of nanoenzymes.

4. Conclusion

Non-antibiotic noble metal nanoparticles can reduce bacterial infection by producing oxidative stress and reducing the emergence of bacteria resistance from overuse of antibiotics. However, traditional materials suffer from problems such as insufficient ROS generation, under-utilization of ROS, and biocompatibility. In this work, a green synthetic strategy is described to produce gold nanoparticles with phenols as the reducing and capping agents and Fe^{3+} for chelation. The nanoparticles adsorb well on the bacterial membranes causing physical stretching. Furthermore, accumulation of pGNP-Fe₂ in the bacteria enhances the oxidase-like functions originating from the gold core and peroxidase-like ability based on the Fenton action arising from chelated Fe^{3+} , leading to the generation of abundant intracellular ROS in situ. In this way, efficient and long-lasting antibacterial effects are accomplished. The versatile ligand described here reveals the large potential of using natural materials to produce non-antibiotic antibacterial materials which capitalize on both chemical and physical effects without needing extraneous antibacterial agents.

5. Experimental Details

Chemicals and Materials: Chloroauric acid ($\text{HAuCl}_4 \cdot 4\text{H}_2\text{O}$) was obtained from Sinopharm Chemical Reagent Co. Ltd. (China) and (+)- catechin hydrate ($\geq 98\%$) and iron chloride hexahydrate ($\text{FeCl}_3 \cdot 6\text{H}_2\text{O}$, 99%) were purchased from Macklin (China). 3,3',5,5'-tetramethylbenzidine (TMB, $\geq 99.0\%$), L-ascorbic acid (AA, 99.7%), dimethyl sulfoxide (DMSO, $\geq 99.9\%$), sodium acetate trihydrate ($\text{C}_2\text{H}_3\text{O}_2\text{Na} \cdot 3\text{H}_2\text{O}$, 99%), and acetic acid (99.8%) were bought from Aladdin (China). All the reagents were used as obtained without purification.

One-Pot Synthesis of pGNP-Fe, pGNP, and pFe: The catechin-stabilized Au/Fe framework (pGNP-Fe) was prepared by a simple and green process involving reduction and coordination. 200 μL of the HAuCl_4 solution (10 mM) were added to 5 mL of the catechin solution (0.05 mM to 0.8 mM increased as double concentration) in a 15 mL centrifuge tube. The solution was mixed gently by shaking up and down several times and kept still for 1 h at room temperature to form the pGNP nanoparticles. Afterwards, 16.8 to 270 μL of FeCl_3 (1 mg mL^{-1}) in geometric progression were added to the solution dropwise for 1 h to perform chelation. The solutions with different concentrations of catechin and FeCl_3 were labeled as pGNP-Fe1, pGNP-Fe2, pGNP-Fe3, pGNP-Fe4, and pGNP-Fe5 (pGNP-Fe) from low to high concentrations. The products were collected after centrifugation at 13000 rpm. The catechin (5 mL, 0.1 mM) reduced Au nanoparticles (designated as pGNP) and catechin (5 mL, 0.1 mM) chelated iron samples (34 μL , 1 mg mL^{-1}) (designated as pFe) were prepared as the control groups. All the solutions were purified by dialysis (MWCO = 8000 for pGNP-Fe and pGNP, MWCO = 100 for pFe) against DI water overnight before further analysis.

Materials Characterization: Transmission electron microscopy (TEM, Philips CM20) and dynamic light scattering particle size analyzer (DLS, Malven Zetasizer Nano ZS) was used to observe the

morphology and hydrodynamic size of the nanoparticle solutions. The chemical composition was determined on a double-beam UV-visible spectrophotometer (Halo DB-20, Dynamica, Australia) and PerkinElmer Spectrum II FTIR spectrometer. The metallic ion concentration was measured by ICP-OES (Optima 8000 spectrometer, PerkinElmer, USA). Taken $[\text{Fe}^{3+}]$ as an example, the pGNP-Fe solution was transferred to an activated dialysis tube (MWCO = 8000) and placed in a 50 mL centrifuge tube which contained deionized water as the hypotonic solution. A certain amount of hypotonic solution was taken out to evaluate the amount of released $[\text{Fe}^{3+}]$ by ICP-OES. The fluorescence intensity was monitored at fixed time points using the Molecular Devices SpectraMax ID5 microplate reader (USA).

Oxidase Activity: The oxidase-like activity was determined with ascorbic acid (AA) as the oxidation model molecule and depletion of AA was characterized by the decreased absorbance peak at 250 nm. In a typical test, 300 μL of pGNP-Fe, pGNP, or pFe ($[\text{Au}] = 40 \text{ mg L}^{-1}$, $[\text{Fe}^{3+}] = 0.8 \text{ mg L}^{-1}$ for pFe) were added to 5 mL of the aqueous AA solution (0.25 mM), respectively, and an appropriate quantity of the solution was collected using a micro-cuvette for UV-vis spectrophotometry.

Oxidative product H_2O_2 was measured to monitor oxidation using the Pierce Quantitative Peroxide Assay and the standard curve was established following the standard protocol. A reaction time of 2 h was chosen to compare the production of H_2O_2 in the different systems. 20 μL of the solution were added to 200 μL of the working reagent on a 96-well plate and the semi-quantitative measurement was carried out by UV-vis spectrophotometry at 595 nm. All the tests were performed three times to improve the statistics.

Peroxidase-Like Activity: The peroxidase-like activity was evaluated by monitoring oxidation of the TMB solution in the presence of hydrogen peroxide. Typically, 20 μL of the specimen were added to the HAc/NaAc buffer (0.2 M, pH = 4.6) containing the TMB solution (4 μL , 100 mM) and H_2O_2 (10 μL , 10 mM) and the final volume was 200 μL after adding the buffer. The major absorbance peak at 652 nm was monitored by UV-vis spectrophotometry. The catalytic kinetics were analyzed by the

Michaelis-Menten equation: $\nu = \frac{V_{\max} [S]}{K_m + [S]}$, where ν is the initial velocity, V_{\max} is the maximum reaction velocity, and $[S]$ is the concentration of substrate. The assay was conducted by varying the concentration of H_2O_2 at a fixed concentration of TMB and the absorbance at 652 nm was recorded on the Biotech Eon microreader in the timescan mode.

The peroxidase-like activity was quantitatively evaluated by detecting production of ROS by staining using the DCFH-DA (Beyotime, China) kit.^[35] The mixture containing 500 μL of DCFH-DA (1 mM in ethanol) and 2 mL of NaOH (0.01 M) was stirred for 30 min at room temperature to obtain the hydrolyzed DCF solution. Afterward, 10 mL of the PBS solution (pH = 7.4) were added to the DCF solution for neutralization and the solution was stored at 4 °C for further analysis. In the typical test, 20 μL of H_2O_2 (10 mM) were added to 140 μL of the sample on a 96-well plate before the addition of 40 μL of the DCF solution. The fluorescence intensity was measured at $\lambda_{\text{ex}} = 488 \text{ nm}$ and $\lambda_{\text{em}} = 530 \text{ nm}$ and three measurements were conducted.

Bacterial Culture and Antibacterial Activity—CFU Counting: The Gram-negative (*Escherichia coli*, ATCC25922) and Gram-positive (*Staphylococcus aureus*, ATCC29213) strains were chosen as the model microorganisms. The *E. coli* cells were cultivated in the LB medium for 12 h in a shaking incubator (220 rpm, 37 °C) and harvested in the exponential growth stage. The bacteria solution was diluted to $\text{OD}_{600} = 0.2$ in the antibacterial test by the spread plate method. Briefly, 800 μL of the bacterial solution (10^5 CFU mL^{-1}) were mixed with 200 μL of the sample ($[\text{Au}] = 40 \text{ mg L}^{-1}$, $[\text{Fe}^{3+}] = 0.8 \text{ mg L}^{-1}$ for pFe) in a shaking incubator (220 rpm, 37 °C) for 1 h, 3 h, and 24 h. The solutions were diluted to gradient concentrations, spread on solid agar plates, and cultivated for another 18 h to count the CFUs. The antibacterial rate was determined by the following formula: Antibacterial rate = $(\text{CFU}_{\text{ctrl}} - \text{CFU}_{\text{exp}}) / \text{CFU}_{\text{ctrl}} \times 100\%$.

Live/Dead Staining: The LIVE/DEAD BacLight Bacterial Viability Kit was used to assess the viability of the bacteria quantitatively. After treating the specimen for 3 h, 3 μL of the mixed dyes were added and

the bacteria were stained for 15 min in darkness at room temperature before centrifugation at 5000 rpm to remove the excess dyes. The bacteria were resuspended in a saline solution, spread on a glass slide, and further sealed with a coverslip for observation. The fluorescent images were captured by an inverted microscope (Axio Observer Z1, Zeiss, Germany). The dead bacteria were stained red ($\lambda_{\text{ex}} = 480\text{--}550\text{ nm}$, $\lambda_{\text{em}} = 590\text{--}800\text{ nm}$) and the live ones were green ($\lambda_{\text{ex}} = 420\text{--}480\text{ nm}$, $\lambda_{\text{em}} = 520\text{--}580\text{ nm}$). Detailed information can be found from previous work.^[36,37]

Morphological Observation: Scanning emission microscopy (SEM) was used to examine the morphology of the bacteria. A silicon wafer was cut into $1 \times 1\text{ cm}$ pieces and cleaned ultrasonically in ethanol. 800 μL of the bacteria solution (10^5 CFU mL^{-1}) were added to 200 μL of the specimen ($[\text{Au}] = 40\text{ mg L}^{-1}$, $[\text{Fe}^{3+}] = 0.8\text{ mg L}^{-1}$ for pFe) and after agitation for 3 h (220 rpm, 37 °C), the bacteria solution was spread on the clean silicon on a 24-well plate for adhesion. After 1 h, the extra solution was removed carefully and the adhered bacteria were fixed with 2.5% glutaraldehyde solution overnight. The samples were then dehydrated with ethanol with concentrations of 10%, 30%, 50%, 70%, 90% and 100% sequentially and dried in a vacuum at 37 °C. Before observation, the specimens were sputter-coated with platinum to reduce charging during SEM.

TEM and EDS were carried out to analyze the microstructure^[38] and elements in the bacteria, respectively.^[6] Briefly, the bacteria were collected by refrigerated centrifugation (5000 rpm for 5 min) and the supernatant was discarded. The precipitate was fixed by embedding in 3% molten agar and immersed in 2.5% glutaraldehyde and 2% paraformaldehyde overnight. After washing with PBS three times, secondary fixation was conducted with 1% OsO₄ for one hour. The gradient PBS solution (0.2, 0.1, 0.05M) and DI water were used to wash the samples. The samples were dehydrated by 30%, 50%, 70%, 80%, 95%, 100%, 100%, 1:1 100% ethanol: acetone, acetone twice, each for 10 min. Infiltration with spurr's resin was performed with rotation and embedding in the plastic mold for half a day and baked in an oven at 70 °C for 2 day before fixing in a copper grid for further examination.

Bacterial Membrane Permeability Assessment: The outer membrane permeability of *E. coli* was evaluated by ANS (8-anilino-1-naphthalene-1-sulfonic acid). The logarithmic phase *E. coli* cells were cultivated for 3 h and diluted to 10^5 CFU mL^{-1} to determine the OD at 600 nm. The final bacterial solution was centrifuged by refrigerating with PBS three times. ANS was added to the bacterial solution and incubated for 20 min at room temperature in the dark. The relative fluorescence intensity was measured on a microplate reader at excitation at 380 nm and emission at 460 nm. The bacterial membrane potential was evaluated by the BacLight Bacterial Membrane Potential Kit (ThermoFisher).^[39] After reacting for 3 h, the bacterial solution was collected and washed three times. The staining process followed the general protocol and fluorescence in the green and red channels are monitored.

Intracellular ROS: 2',7'-dichlorodihydrofluorescein diacetate (H_2DCFDA , Thermo Fisher Scientific, USA) was introduced to determine the intracellular ROS level. After incubation with the specimen for 3 h, 1 μL of the H_2DCFDA solution (10 mM) was added and stained for 15 min in darkness. The solution was centrifuged at 5000 rpm to remove the extra dye in the supernatant and the precipitate was re-dispersed in 1 mL of the PBS solution. 5 μL of the solution were spread on a glass slide for qualitative observation under an inverted microscope ($\lambda_{\text{ex}} = 420\text{--}480\text{ nm}$, $\lambda_{\text{em}} = 520\text{--}580\text{ nm}$). A microplate reader was employed to monitor the fluorescence intensity at the designated time points at $\lambda_{\text{ex}} = 488\text{ nm}$ and $\lambda_{\text{em}} = 530\text{ nm}$. All the measurements were conducted in triplicate.

Statistical Analysis: The experimental results were presented as mean \pm standard deviation ($n = 3$). The differences among groups were analyzed by the one-way ANOVA using Statistical Package for Social Sciences (SPSS) software. The asterisks signify statistically significant differences (* $p < 0.05$, ** $p < 0.01$, and *** $p < 0.001$).

Supporting Information

Supporting Information is available from the Wiley Online Library or from the author.

Acknowledgements

Financial support from Shenzhen – Hong Kong Innovative Collaborative Research and Development Program (No. 9240014), City University of Hong Kong Strategic Research Grant (SRG) No. 7005505 and HK Tech 300 Seed Fund (SF202109169) is acknowledged.

Conflict of Interest

The authors declare no conflict of interest.

Data Availability Statement

The data that support the findings of this study are available on request from the corresponding author. The data are not publicly available due to privacy or ethical restrictions.

Keywords

antibacterial effects, enzyme-like properties, gold nanoparticles, Polyphenol-incorporated nanoframe, reactive oxygen species

Received: October 20, 2021

Revised: January 7, 2022

Published online: March 4, 2022

- [1] Y. Wang, Y. Yang, Y. Shi, H. Song, C. Yu, *Adv. Mater.* **2020**, *32*, 1904106.
- [2] M. P. Brynildsen, J. A. Winkler, C. S. Spina, I. C. MacDonald, J. J. Collins, *Nat. Biotechnol.* **2013**, *31*, 160.
- [3] H. Van Acker, T. Coenye, *Trends Microbiol.* **2017**, *25*, 456.
- [4] X. Yang, J. Li, T. Liang, C. Ma, Y. Zhang, H. Chen, N. Hanagata, H. Su, M. Xu, *Nanoscale* **2014**, *6*, 10126.
- [5] Q. Zheng, X. Liu, Y. Zheng, K. W. Yeung, Z. Cui, Y. Liang, Z. Li, S. Zhu, X. Wang, S. Wu, *Chem. Soc. Rev.* **2021**, *50*, 5086.
- [6] X. Xie, C. Mao, X. Liu, L. Tan, Z. Cui, X. Yang, S. Zhu, Z. Li, X. Yuan, Y. Zheng, *ACS Cent. Sci.* **2018**, *4*, 724.
- [7] W. Guan, L. Tan, X. Liu, Z. Cui, Y. Zheng, K. W. K. Yeung, D. Zheng, Y. Liang, Z. Li, S. Zhu, *Adv. Mater.* **2021**, *33*, 2006047.
- [8] Y. Tao, E. Ju, J. Ren, X. Qu, *Adv. Mater.* **2015**, *27*, 1097.
- [9] A. Balfourier, J. Kolosnjaj-Tabi, N. Luciani, F. Carn, F. Gazeau, *Proc. Natl. Acad. Sci. USA* **2020**, *117*, 22639.
- [10] J. Zhou, Z. Lin, Y. Ju, M. A. Rahim, J. J. Richardson, F. Caruso, *Acc. Chem. Res.* **2020**, *53*, 1269.
- [11] P. Orłowski, M. Zmigrodzka, E. Tomaszewska, K. Ranoszek-Soliwoda, B. Pajak, A. Slonska, J. Cymerys, G. Celichowski, J. Grobelny, M. Krzyzowska, *Int. J. Nanomed.* **2020**, *15*, 4969.
- [12] Y. Hu, H. Cheng, X. Zhao, J. Wu, F. Muhammad, S. Lin, J. He, L. Zhou, C. Zhang, Y. Deng, P. Wang, Z. Zhou, S. Nie, H. Wei, *ACS Nano* **2017**, *11*, 5558.
- [13] V. Kumar, D. Bano, D. K. Singh, S. Mohan, V. K. Singh, S. H. Hasan, *ACS Sustainable Chem. Eng.* **2018**, *6*, 7662.
- [14] M. E. Hafez, H. Ma, W. Ma, Y. T. Long, *Angew. Chem., Int. Ed.* **2019**, *131*, 6393.
- [15] C. Jiang, S. Pang, F. Ouyang, J. Ma, J. Jiang, *J. Hazard. Mater.* **2010**, *174*, 813.
- [16] D. P. Linklater, V. A. Baulin, X. Le Guével, J. B. Fleury, E. Hanssen, T. H. P. Nguyen, S. Juodkazis, G. Bryant, R. J. Crawford, P. Stoodley, *Adv. Mater.* **2020**, *32*, 2005679.
- [17] E. C. Dreaden, A. M. Alkilany, X. Huang, C. J. Murphy, M. A. El-Sayed, *Chem. Soc. Rev.* **2012**, *41*, 2740.

- [18] J. Guo, B. L. Tardy, A. J. Christofferson, Y. Dai, J. J. Richardson, W. Zhu, M. Hu, Y. Ju, J. Cui, R. R. Dagastine, I. Yarovsky, F. Caruso, *Nat. Nanotechnol.* **2016**, *11*, 1105.
- [19] W. Haiss, N. T. Thanh, J. Aveyard, D. G. Fernig, *Anal. Chem.* **2007**, *79*, 4215.
- [20] I. C. Chiang, D. H. Chen, *Adv. Funct. Mater.* **2007**, *17*, 1311.
- [21] M. Comotti, C. Della Pina, R. Matarrese, M. Rossi, *Angew. Chem., Int. Ed.* **2004**, *43*, 5812.
- [22] J. Nielsen, *Nat. Prod. Rep.* **2019**, *36*, 1233.
- [23] A. Plauack, E. E. Stangland, J. A. Dumesic, M. Mavrikakis, *Proc. Natl. Acad. Sci. USA* **2016**, *113*, E1973.
- [24] Q. Zhang, S. Chen, H. Wang, *Green Chem.* **2018**, *20*, 4067.
- [25] X. Mei, T. Hu, H. Wang, R. Liang, W. Bu, M. Wei, *Biomaterials* **2020**, *258*, 120257.
- [26] C. Zhang, B. Wu, Y. Zhou, F. Zhou, W. Liu, Z. Wang, *Chem. Soc. Rev.* **2020**, *49*, 3605.
- [27] Y. Beldjoudi, A. Atilgan, J. A. Weber, I. Roy, R. M. Young, J. Yu, P. Deria, A. E. Enciso, M. R. Wasielewski, J. T. Hupp, J. F. Stoddart, *Adv. Mater.* **2020**, *32*, 2070237.
- [28] W. Zhang, X. Ren, S. Shi, M. Li, L. Liu, X. Han, W. Zhu, T. Yue, J. Sun, J. Wang, *Nanoscale* **2020**, *12*, 16330.
- [29] X. Liu, Z. Yan, Y. Zhang, Z. Liu, Y. Sun, J. Ren, X. Qu, *ACS Nano* **2019**, *13*, 5222.
- [30] Z. Zhao, D. C. Pan, Q. M. Qi, J. Kim, N. Kapate, T. Sun, C. W. T. Shields, L. L. Wang, D. Wu, C. J. Kwon, W. He, J. Guo, S. Mitragotri, *Adv. Mater.* **2020**, *32*, 2003492.
- [31] T. Lin, Y. Qin, Y. Huang, R. Yang, L. Hou, F. Ye, S. Zhao, *Chem. Commun.* **2018**, *54*, 1762.
- [32] X. Ruan, D. Liu, X. Niu, Y. Wang, C. D. Simpson, N. Cheng, D. Du, Y. Lin, *Anal. Chem.* **2019**, *91*, 13847.
- [33] D. P. Linklater, V. A. Baulin, X. Le Guevel, J. B. Fleury, E. Hanssen, T. H. P. Nguyen, S. Juodkasis, G. Bryant, R. J. Crawford, P. Stoodley, E. P. Ivanova, *Adv. Mater.* **2020**, *32*, 2005679.
- [34] K. Kajiya, H. Hojo, M. Suzuki, F. Nanjo, S. Kumazawa, T. Nakayama, *J. Agric. Food Chem.* **2004**, *52*, 1514.
- [35] A. Punjabi, X. Wu, A. Tokatli-Apollon, M. El-Rifai, H. Lee, Y. Zhang, C. Wang, Z. Liu, E. M. Chan, C. Duan, G. Han, *ACS Nano* **2014**, *8*, 10621.
- [36] G. Wang, K. Tang, Z. Meng, P. Liu, S. Mo, B. Mehrjou, H. Wang, X. Liu, Z. Wu, P. K. Chu, *Adv. Mater.* **2020**, *32*, 2003616.
- [37] G. Wang, H. Feng, L. Hu, W. Jin, Q. Hao, A. Gao, X. Peng, W. Li, K.-Y. Wong, H. Wang, *Nat. Commun.* **2018**, *9*, 2055.
- [38] G. Wang, W. Jiang, S. Mo, L. Xie, Q. Liao, L. Hu, Q. Ruan, K. Tang, B. Mehrjou, M. Liu, L. Tong, H. Wang, J. Zhuang, G. Wu, P. K. Chu, *Adv. Sci.* **2020**, *7*, 1902089.
- [39] G. Wang, W. Jin, A. M. Qasim, A. Gao, X. Peng, W. Li, H. Feng, P. K. Chu, *Biomaterials* **2017**, *124*, 25.

Supporting Information

for *Adv. Funct. Mater.*, DOI: 10.1002/adfm.202110635

Versatile Phenol-Incorporated Nanoframes for In Situ
Antibacterial Activity Based on Oxidative and Physical
Damages

*Pei Liu, Yuzheng Wu, Babak Mehrjou, Kaiwei Tang,
Guomin Wang,* and Paul K. Chu**

Supporting Information

Versatile phenol-incorporated nanoframes for *in situ* antibacterial activity based on oxidative and physical damages

Pei Liu, Yuzheng Wu, Babak Mehrjou ,Kaiwei Tang, Guomin Wang, Paul K. Chu**

Department of Physics, Department of Materials Science and Engineering, and
Department of Biomedical Engineering, City University of Hong Kong, Tat Chee
Avenue, Kowloon, Hong Kong 999077, China

* Corresponding authors: E-mail: guomiwang2-c@my.cityu.edu.hk (G. M. Wang);
paul.chu@cityu.edu.hk (P. K. Chu)

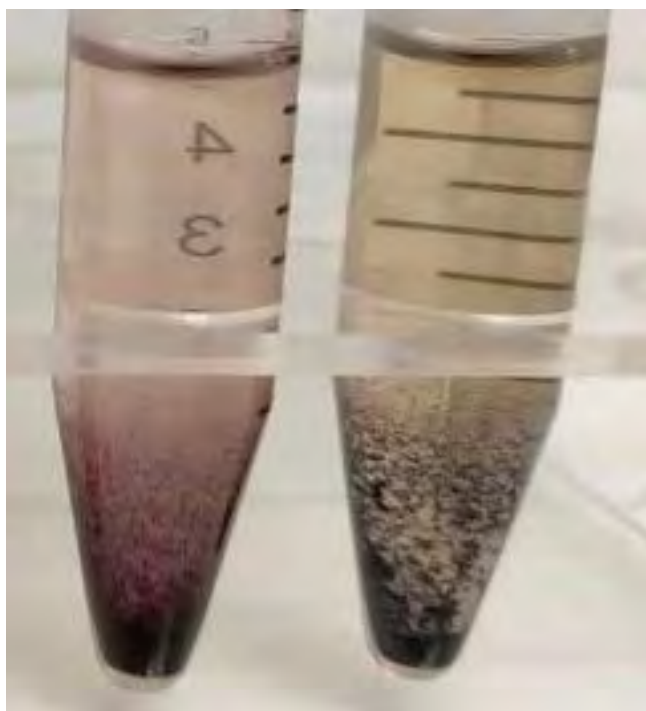


Figure S1. Optical images of pGNP-Fe4 ([catechin]=0.4 mM, left) and pGNP-Fe5 ([catechin]=0.8 mM, right) with different concentrations of catechin.

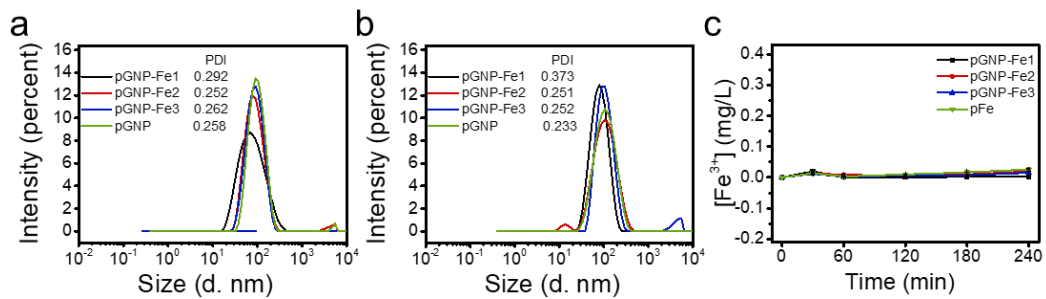


Figure S2. Stability assessment: DLS measurement for (a) 1 day and (b) 7 days (b): (c)

Released Fe^{3+} determined by ICP-OES.

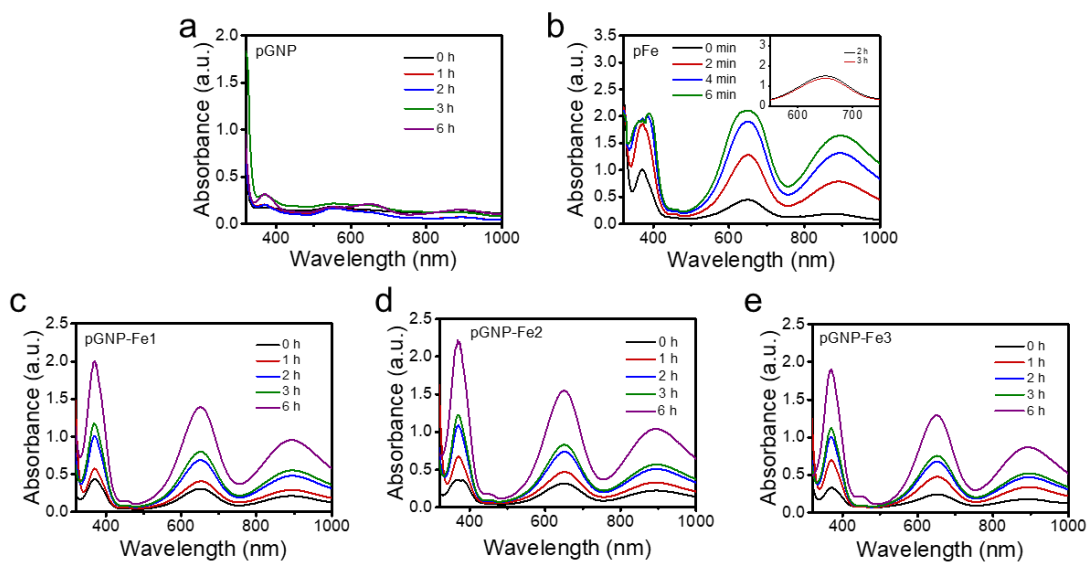


Figure S3. Time-dependent oxidase-like properties determined by catalyzing AA: (a) pFe, (b) pGNP, (c) pGNP-Fe1, (d) pGNP-Fe2, and (e) pGNP-Fe3.

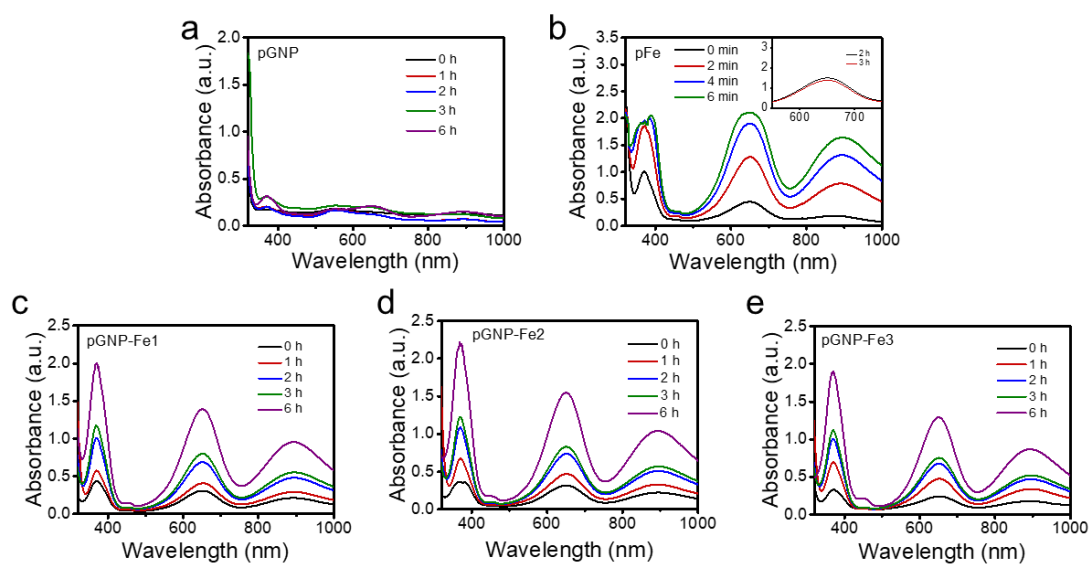


Figure S4. Time-dependent peroxidase-like properties of catalytic oxidation of TMB with H_2O_2 : (a) pFe, (b) pGNP, (c) pGNP-Fe1, (d) pGNP-Fe2, and (e) pGNP-Fe3.

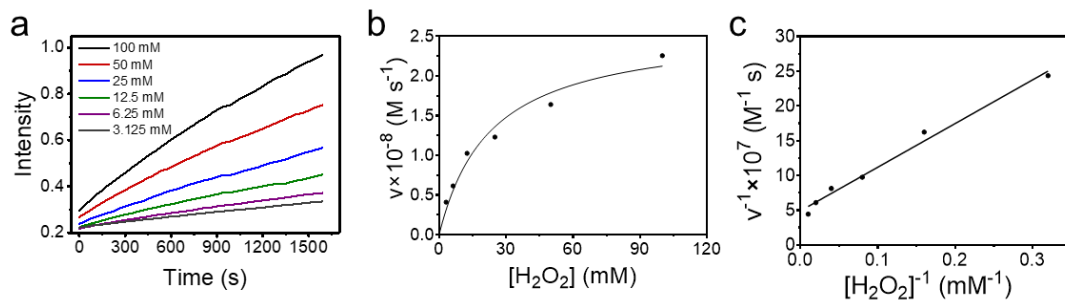


Figure S5. Enzyme kinetics of pGNP-Fe2: (a) Absorbance at 652 nm with time for different H₂O₂ concentrations and 1 mM TMB (pH = 4.2); (b) Michaelis-Menten fitting and (c) Lineweaver-Burk fitting for different H₂O₂ concentrations.

Table S1. Comparison of the kinetics parameter of K_m and V_{max} .

	Substrate	K_m (mM)	V_{max} ($M s^{-1}$)
pGNP-Fe2 (this work)	H_2O_2	23	2.61×10^{-8}
Fe_3O_4 MNPs	H_2O_2	154	9.78×10^{-8}
HRP	H_2O_2	3.7	8.71×10^{-8}

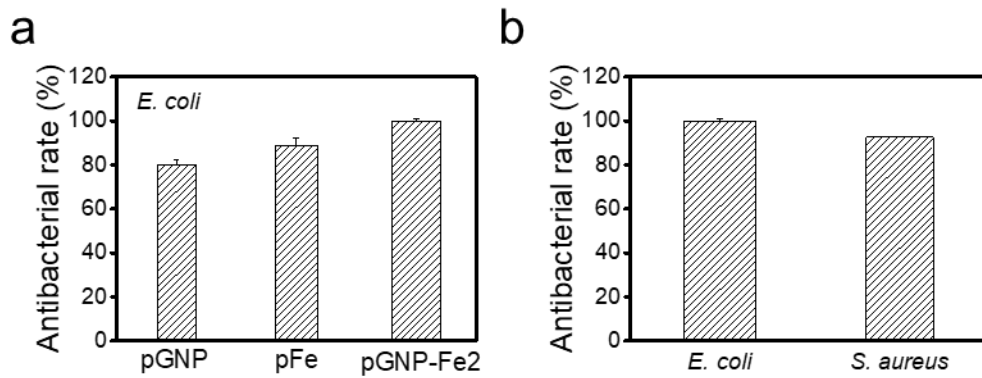


Figure S6. (a) Antibacterial rates of different samples against *E.coli* after culturing for 24 h and (b) Comparison of the antibacterial rates of pGNP-Fe2 against *E. coli* and *S. aureus* after 24 h.

Reference:

1. Gao, L.; Zhuang, J.; Nie, L.; Zhang, J.; Zhang, Y.; Gu, N.; Wang, T.; Feng, J.; Yang, D.; Perrett, S.; Yan, X., *Nat Nanotechnol.* **2007**, *2*, 577.